

ARTICLE OPEN



Design and fabrication of a stable Ni-PTFE-SiC superhydrophobic anticorrosive coating by electrodeposition

Jianguo Liu¹✉, Xiuting Fang^{1,2}, Huixiang Ma², Jie Cheng³, Xiao Xing¹, Gan Cui¹✉ and Zili Li¹

Superhydrophobic coatings show great application potential in many fields, but they have not been widely used due to poor stability. A Ni-PTFE-SiC composite coating was proposed in this paper. Firstly, the Ni-PTFE-SiC coating structure was designed by molecular dynamics simulations. The feasibility of superhydrophobic effect of this structure and the adsorption stability of the composite coatings were proved. This approach can also be used to avoid trial and errors when selecting other similar candidate substances. Then, the Ni-PTFE-SiC superhydrophobic coatings were successfully prepared by composite electrodeposition, with the water contact angle of more than 155° and the sliding angle of close to 0°. The effects of current density, deposition time and nanoparticle concentration on the wettability and morphology of the coatings were also investigated. Through comparative experiments, the best preparation parameters were: PTFE 14 g L⁻¹, SiC 6 g L⁻¹, primary current density 7 A dm⁻² (10 min) and secondary current density 15 A dm⁻² (5 min). This preparation method doesn't need additional modification with low surface energy substances like the traditional preparation process, and greatly improves the corrosion resistance, wear resistance and durability of the coatings.

npj Materials Degradation (2023)7:90; <https://doi.org/10.1038/s41529-023-00412-y>

INTRODUCTION

In recent years, superhydrophobic coatings have attracted considerable attention because of their potential in many fields¹, such as anti-corrosion^{2–4}, oil-water separation⁵, prevention of biofilm⁶, anti-icing⁷, anti-fogging⁸ and so on⁹. However, superhydrophobic coatings have the fatal defect of poor stability, which prevents them from being widely used in practical applications. On the one hand, the realization of the superhydrophobic effect usually relies on the micro-nano structures on the surface, but these structures are relatively fragile and easily destroyed by external forces^{7,10,11}. On the other hand, existing preparation processes often require surface modification with low surface energy substances, while these substances will peel off under slight abrasion, resulting in loss of superhydrophobicity. Therefore, improving the stability of superhydrophobic coatings has become the key technology these days.

Composite electrodeposition undoubtedly provides a way to solve the problem of poor stability of superhydrophobic coatings, including corrosion resistance, wear resistance and durability. The so-called composite electrodeposition is that some particles with special properties are added to the plating bath and co-deposited with the matrix, so that the coating can have the advantages of both matrix and particles¹². The most common matrix is metal. For example, Zhou et al.¹³ prepared Ni-based composite coatings embedded with MoS₂ nanoparticles, a solid lubricant, which had been proved to achieve a lower coefficient of friction and enhanced wear resistance. By controlling the current density during the electrodeposition process, Wang et al.¹⁴ prepared Cu-CNTs composite coatings with carbon nanotubes uniformly distributed in the Cu matrix, which obtained high strength and good ductility. Based on the advantages of WC and WS₂ nanoparticles, the Ni-WC-WS₂ coatings prepared by composite electrodeposition simultaneously obtained high hardness, self-

lubricity and excellent corrosion resistance¹⁵. In this way, if two different particles with wear resistance and low surface energy are added to the matrix at the same time, the good hydrophobicity and high stability of the coatings can be achieved by one-step electrodeposition without surface modification.

As a substance with a hardness slightly lower than that of diamond, SiC particles have been widely utilized to co-deposition with metals to improve their tribological properties^{16–20}. Zhang et al.¹⁶ prepared Ni-SiC composite coating by ultrasonic electrodeposition, exhibiting a microhardness of 715.7 HV, while the microhardness of pure Ni coatings was only 485.8 HV. Wasekar et al.²⁰ found that the maximum hardness of Ni-W-SiC composite coatings increased by 25% compared with Ni-W alloy. Polytetrafluoroethylene (PTFE) is the self-lubricating material with the lowest friction coefficient found so far, which makes it extensively used to prepare self-lubricating coatings with good wear resistance. Meanwhile, PTFE has the lowest surface energy with surface tension of only about 0.019 N m⁻¹, which is beneficial to the manufacture of superhydrophobic surfaces. Jiang et al.²¹ prepared Ni-PTFE-SiC composite coating, the adhesion strength and corrosion resistance were enhanced by multi-physics coupled deposition, the surface wettability of the coating was not considered. Wu et al.²² prepared Ni-P-PTFE-SiC composite coating, which demonstrates a combination of the advantages of the Ni-P-SiC in high hardness and wear resistance, and of the Ni-P-PTFE coating in a low friction coefficient, lower surface energy. The contact angle was 103°. Huang et al.²³ prepared Ni-P-PTFE-SiC composite coating, the contact angle was 101.7°. Daniel et al.²⁴ prepared Ni-PTFE superhydrophobic coatings on copper substrates by adding PTFE nanoparticles to Watts bath, and the maximum contact angle reached 152°. Later, they proved that the Ni-PTFE superhydrophobic coatings had good abrasion resistance and thermal stability through linear wear test²⁵ and heat

¹Shandong Key Laboratory of Oil & Gas Storage and Transportation Safety, College of Pipeline and Civil Engineering, China University of Petroleum (East China), 266580 Qingdao, China. ²China Petroleum Pipeline Engineering Co. Ltd, 065000 Langfang, China. ³Changqing Engineering Design Co. Ltd, 710018 Xi'an, China. ✉email: liujianguo@upc.edu.cn; chennacuigan@163.com

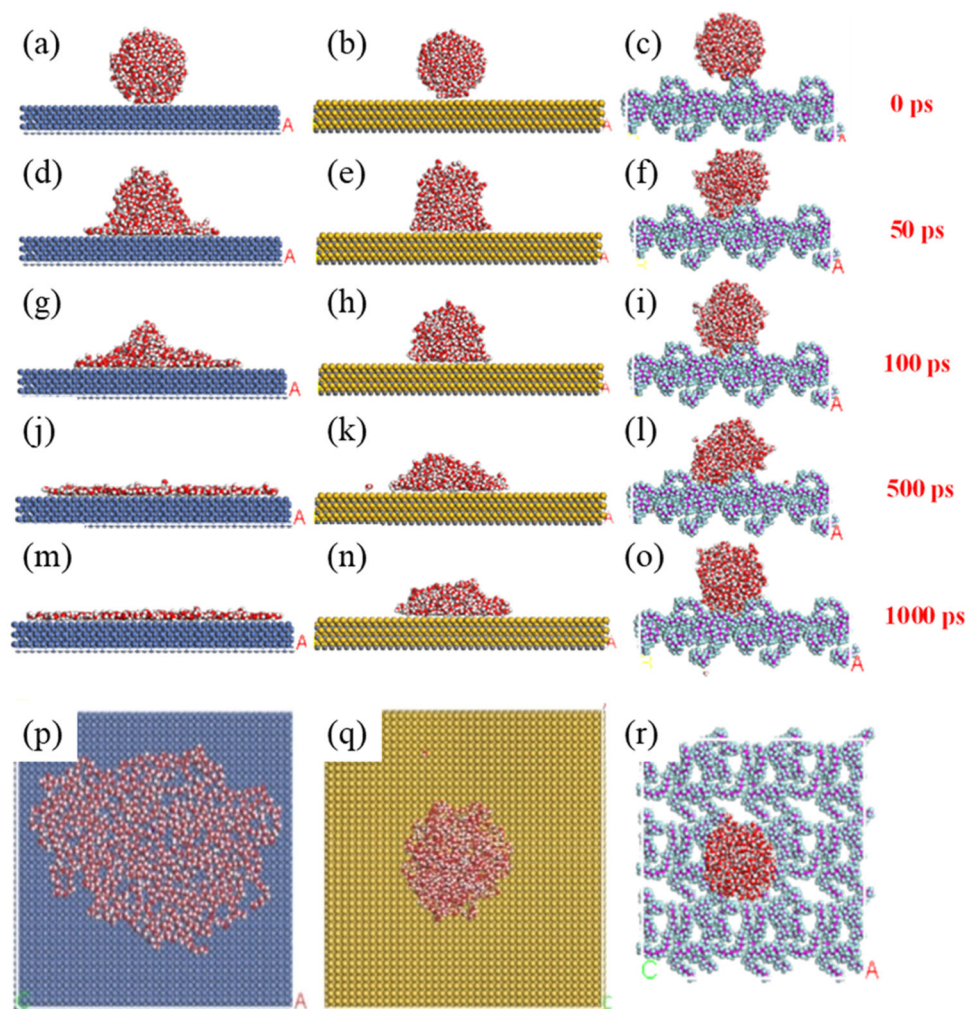


Fig. 1 Wetting stater of water droplets on the different surface. Wetting stater of (a) Ni matrix, (b) SiC matrix and (c) PTFE matrix at 0 ps, (d) Ni matrix, (e) SiC matrix and (f) PTFE matrix at 50 ps, (g) Ni matrix, (h) SiC matrix and (i) PTFE matrix at 100 ps, (j) Ni matrix, (k) SiC matrix and (l) PTFE matrix at 500 ps, (m) Ni matrix, (n) SiC matrix and (o) PTFE matrix at 1000 ps; (p), (q) and (r) are the corresponding top views of (m), (n) and (o).

resistance test²⁶ respectively. Other literatures^{27–29} have also paid attention to the superhydrophobicity of metal-based-PTFE composite coatings fabricated by one step electrodeposition.

With the development of computer technology, molecular dynamics (MD) simulations have played an important role in exploring surface and interface properties, analyzing reaction mechanisms, guiding substance synthesis, drug design and other fields. By simulating the wetting behavior of droplets on the surface of certain material, it can provide a powerful guidance for structural design of coatings. For instance, Sethi et al.³⁰ simulated the wetting configuration of water droplets and oil droplets on the coatings composed of PDMS and different hydrolysis contents of PVAc by MD simulations. They also calculated the contact angle of droplets and the adsorption energy between coatings and substrates to determine the best coating composition. Kitabata et al.³¹ simulated the wetting behavior of water droplets on both crystal and amorphous PVDF surfaces to explore the effect of microstructure on surface wettability. In addition, MD simulations can also be used to explore the adsorption stability and self-diffusion of membranes³².

This paper aims to prepare Ni-PTFE-SiC anticorrosive superhydrophobic coatings with high stability by electrodeposition without surface modification. Firstly, the preliminary design of the coating was carried out using MD simulations, including the

wetting behavior of water droplets on the surface of Ni, SiC and PTFE to investigate the effect of these two kinds of nanoparticles on the wettability of coatings. Secondly, the adsorption of Ni-PTFE-SiC film on Fe matrix was studied by MD simulations to find out whether the composite coatings can adsorb stably on the substrate. Then, the superhydrophobic coatings were fabricated by controlling the current density, the deposition time and the content of nanoparticles in the bath. In addition, a modified coating was made using myristic acid as surface modifier, which is often used to create superhydrophobic surface due to its low surface energy. Finally, the stability of the modified coatings and the Ni-PTFE-SiC composite coatings were compared, including their corrosion resistance, wear resistance and durability.

RESULTS AND DISCUSSION

Wetting behavior of water droplets

The dynamic wetting behavior of water droplets on the surface of three pure substances at different times is shown in Fig. 1. It can be seen from Fig. 1a, d, g, j, m, that the water molecules on the smooth nickel surface spread down rapidly, and a water film had been formed on the surface at 500 ps. Subsequently, water molecules continued to migrate on the nickel surface, which indicated that the smooth nickel matrix itself had strong

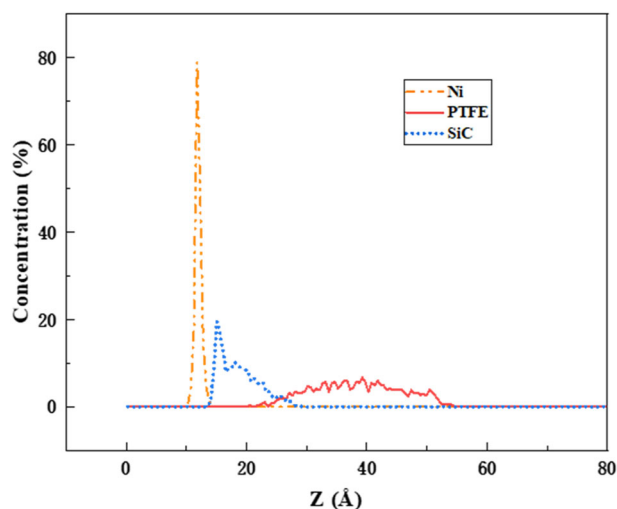


Fig. 2 Concentration of water molecules along the Z axis on different substrates.

hydrophilicity. When the water droplet was on the SiC surface, as shown in Fig. 1b, e, h, k, n, the spreading speed of water molecules was relatively slow and the final WCA was obviously less than 90° , which proved that the hydrophobicity of smooth SiC surface was slightly stronger than that of metal Ni, but it was still hydrophilic. When the water droplet was located on the surface of PTFE, as depicted in Fig. 1c, f, i, l, o, the water molecules only moved very slowly downward under the action of gravity, but hardly spread along the matrix. The hydrophobic long chain of PTFE molecules inserted into the water droplet and prevented the water molecules from migrating to the surface of the matrix, resulting in the final WCA much greater than 90° , indicating that PTFE had strong hydrophobicity. Figure 1p illustrates the top view of the water droplets when they reached equilibrium on the surface of the three substances. Obviously, the spreading area of water droplets on the Ni surface was large, followed by SiC, while the spreading area of water droplets on the PTFE surface was very small and the water molecules were still closely adsorbed together.

Figure 2 shows the concentration distribution of water molecules on the surface of different substrates along the Z axis. It can be seen that the peak point of water molecules appeared at about 11.8 \AA from the Ni surface and the relative concentration was as high as 80%, that is, a large number of water molecules gathered in a very narrow height range close to the Ni substrate to form a water film. On the SiC substrate, water molecules were mainly distributed in the range of 14 \AA to 29 \AA from the surface, accompanied by the first high concentration peak at 15.2 \AA and the second peak at 18.8 \AA . On the surface of PTFE, the concentration distribution of water molecules did not show a clear peak, but rather evenly distributed in an extremely wide range of 20.5 \AA to 55 \AA from the surface, indicating the strong hydrophobic ability of PTFE.

The interaction energy between the droplet and the surface of a certain material is also an important parameter that affects its wetting behavior. It is generally believed that the smaller the interaction energy, the more difficult it is for water molecules to adsorb on the substrate, indicating that the surface of the material is more hydrophobic³³. Therefore, calculating the interaction energy between water droplets and the substrate can also provide a theoretical basis for predicting the wettability of a certain material. The interaction energy between the droplet and the substrate can be calculated according to Eq. (1):³⁴

$$E_{\text{interaction}} = E_{\text{total}} - (E_{\text{surface}} + E_{\text{liquid}}) \quad (1)$$

Table 1. Interaction energy between water droplets and different substrates.

matrix	Ni	SiC	PTFE
$E_{\text{interaction}}(\text{kcal mol}^{-1})$	-1626.960	-251.339	-28.036
$E_{\text{vaw}}(\text{kcal mol}^{-1})$	-1626.955	-251.293	-22.466
$E_{\text{ele}}(\text{kcal mol}^{-1})$	-0.004	-0.045	-5.570

where $E_{\text{interaction}}$ is the interaction energy between the droplet and the substrate. E_{total} is the total energy of the whole system. E_{surface} is the energy of the substrate without adsorbing the droplet and E_{liquid} is the energy of the droplet. Similarly, the van der Waals interaction E_{vaw} and electrostatic interaction E_{ele} between droplets and matrix can be obtained by the same algorithm.

Table 1 shows the calculation results of $E_{\text{interaction}}$, E_{vaw} and E_{ele} between water droplets and different substrates. It can be seen that the energy between the water droplets and the surfaces of the three substrates was all negative, indicating that there was an attraction between them. The interaction energy between the water droplet and the Ni matrix was as high as $-1626.960 \text{ kcal mol}^{-1}$, much higher than that between the water droplet and the other two substrates, which were $-251.339 \text{ kcal mol}^{-1}$ and $-28.036 \text{ kcal mol}^{-1}$, respectively. Therefore, with the decrease of $E_{\text{interaction}}$ value, the spreading ability of the water droplet on the surface of the three kinds of matrix decreased successively. In addition, the data in Table 1 shows that the energy composition between the water droplet and the substrate mainly came from the van der Waals force between the molecules, while the electrostatic interaction accounted for a very small proportion.

In summary, the hydrophobicity of SiC and PTFE was stronger than that of metallic nickel, so the introduction of these two kinds of nanoparticles in the coatings would be more conducive to the realization of the superhydrophobic effect.

Adsorption stability of coatings

Figure 3 shows the adsorption process of myristic acid molecules on the Ni surface. It can be seen that the myristic acid molecules were disorderly distributed at the initial moment, and then gradually move downward, forming the first regular molecular layer next to the Ni matrix. Later, the excess myristic acid molecules continued to adsorb above the first adsorption layer to form the second adsorption layer. As shown in Fig. 3b, the first dense adsorption layer had been formed at 250 ps, but the distribution of top molecules was still disordered. From 500 ps, as shown in Fig. 3c, d, the long chain of myristic acid molecules gradually spread out until the formation of the second adsorption layer. However, compared with the first layer, the density of the second adsorption film had decreased visibly.

Figure 4 shows the adsorption process of Ni-PTFE-SiC composite film on the Fe surface. Compared with Fig. 4a, b is the simulation system after structural optimization, from which it can be seen that the obvious gap between the Fe matrix and the composite layer had disappeared, indicating that there was a strong attraction between iron atoms and nickel atoms. Subsequently, the three substances all showed a tendency to continue to move towards the surface of the Fe matrix, especially the nickel atoms, which were rapidly deposited and arranged regularly, and metal bonds were formed between the Ni-Fe, as shown in Fig. 4d.

Similar to Eq. (1), the adsorption energy of the myristic acid adsorption film and the metal nickel surface was calculated to be $-2208.215 \text{ kcal mol}^{-1}$, all from the intermolecular force—van der Waals interaction, and the electrostatic attraction between the two was also 0. In other words, the myristic acid molecules cannot form chemical bonds with the nickel surface, but only relied on

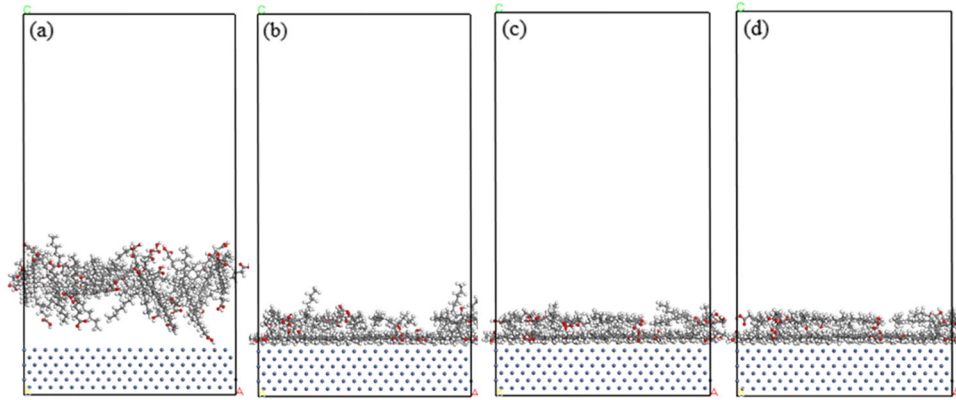


Fig. 3 Adsorption process of myristic acid on Ni matrix. Adsorption at (a) 0 ps, (b) 250 ps, (c) 500 ps and (d) 1000 ps.

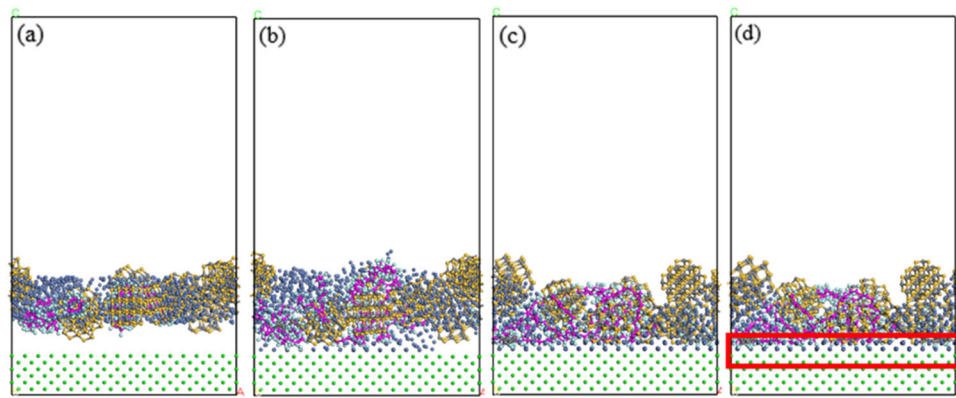


Fig. 4 Adsorption process of Ni-PTFE-SiC layer on Fe matrix. Adsorption (a) before structural optimization, at (b) 0 ps, (c) 500 ps and (d) 1000 ps.

van der Waals force to form physical adsorption, which also revealed the inherent reason for the poor durability of the modified superhydrophobic coatings. While, SiC and PTFE particles were tightly wrapped by nickel atoms, which then formed stronger metal bonds with iron atoms, so the composite film could be more stably adsorbed on the substrate.

The self-diffusion of the coatings is another important factor affecting their stability. Taking $R_i(t)$ and $R_i(0)$ as the positions of particle i at time t and 0 respectively, the average square of displacement is called mean square displacement (MSD)^{35,36}, as shown in Eq. (2). The small slope of the MSD curve means that the material diffuses slowly and the coating is more stable. Conversely, the larger the slope of the MSD curve is, the more intense the particle diffusion is, which means that the stability of the film is worse.

$$\text{MSD} = \langle [R_i(t) - R_i(0)]^2 \rangle \quad (2)$$

Figure 5 shows the MSD curves of myristic acid molecules, Ni atoms, PTFE and SiC particles in the Ni-PTFE-SiC composite coatings, respectively. It can be observed that there was a clear difference between the migration process of the myristic acid molecules and the substances in the composite coatings. First, the MSD curve of the myristic acid molecules was apparently divided into two segments, which corresponded to the layered adsorption observed in the adsorption configuration. Secondly, the MSD curve of the myristic acid molecules was always above the curves of the other three molecules, indicating that the migration amplitude of the former was greater than the latter. Last but

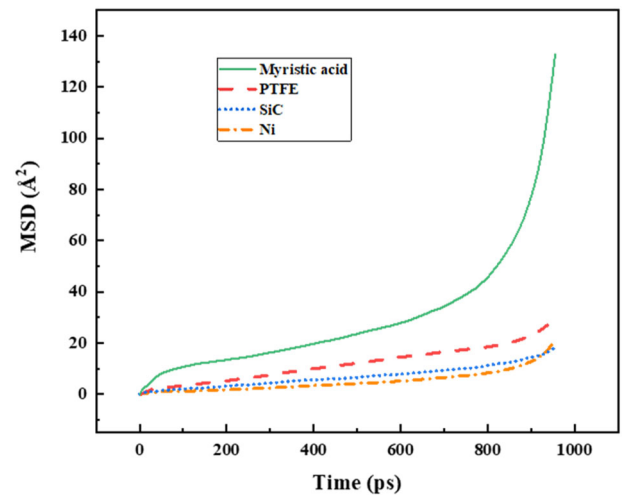


Fig. 5 Mean square displacement curves of different substances.

not least, the MSD curves of Ni atoms, PTFE and SiC particles had similar trends, and their slopes had little difference and were much smaller than that of myristic acid, indicating that the three substances did form a complete composite film and the diffusion rate of this film was significantly lower than that of the modifier one.

The self-diffusion coefficient D of the film can be calculated by the Einstein diffusion formula (Eq. (3)), where N_a is the number of

diffused particles. By calculation, the diffusion coefficient of the myristic acid modified layer (average of two segments) was $6.793 \times 10^{-10} \text{ m}^2 \text{ s}^{-1}$, while the diffusion coefficient of the Ni-PTFE-SiC composite coating (average value of Ni, PTFE and SiC) was only $2.591 \times 10^{-11} \text{ m}^2 \text{ s}^{-1}$, which was about 1/26 of the former, suggesting that the composite coating diffused much more slowly.

$$D = \frac{1}{6N_a} \lim_{t \rightarrow \infty} \frac{d}{dt} \sum_{i=1}^{N_a} \langle [R_i(t) - R_i(0)]^2 \rangle \quad (3)$$

To sum up, the adhesion between the myristic acid modified film and the Ni surface was small and the self-diffusion was intense, while the Ni-PTFE-SiC composite film had a large adhesion

to the Fe matrix and slow self-diffusion, which would make the stability of the Ni-PTFE-SiC superhydrophobic coatings much higher than that of the surface modified superhydrophobic coatings.

The MD simulation results of the wetting behavior of water droplets on different substrates show that the water droplets spread on the metal Ni surface to form a water film, while the contact angles formed on the surface of SiC and PTFE were acute and obtuse angles, respectively, and the adsorption energy between water molecules and the surface of Ni, SiC and PTFE decreased sequentially. Therefore, the hydrophobicity of the three substances ranging from strong to weak was PTFE > SiC > Ni. The embedding of PTFE and SiC nanoparticles contributed to the superhydrophobicity of the coating.

Fabrication of superhydrophobic coatings

MD simulations proved the advantages and feasibility of Ni-PTFE-SiC composite coating structure from two aspects of wettability and adsorption stability, and then the superhydrophobic coatings were successfully prepared by electrodeposition. At the same time, the effects of different process parameters on the properties of the coatings were investigated.

Figure 6 shows the WCA and SA of pure nickel coatings without nanoparticles prepared at different current densities, in which the horizontal axis coordinate "7 + 15" represents a current density of 7 A dm^{-2} for 20 min, followed by a secondary electrodeposition for 5 min at a current density of 15 A dm^{-2} . Other groups were only electrodeposited for 20 min at the corresponding current densities. When only one-step electrodeposition was carried out, the WCA increased at first and then decreased with the increase of current density. Correspondingly, the changing trend of SA was just the opposite. Specifically, the WCA of the nickel coatings was only about 55° and the SA was nearly 40° at a current density of 1 A dm^{-2} . As the current density increased to 7 A dm^{-2} , the WCA reached more than 90° , and the coatings changed from

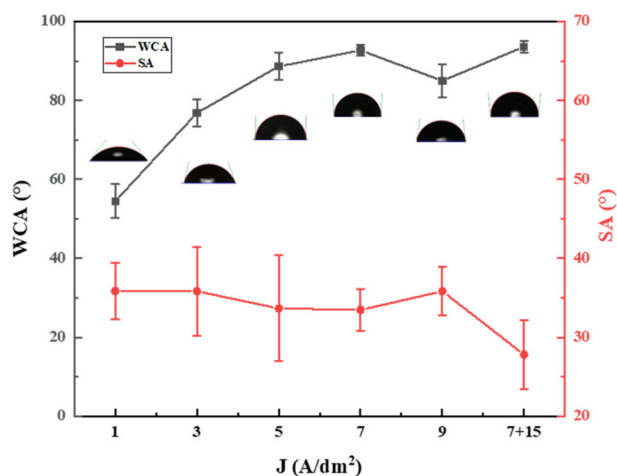


Fig. 6 WCA and SA of pure Ni coatings at different current densities. The error bars indicate standard deviations.

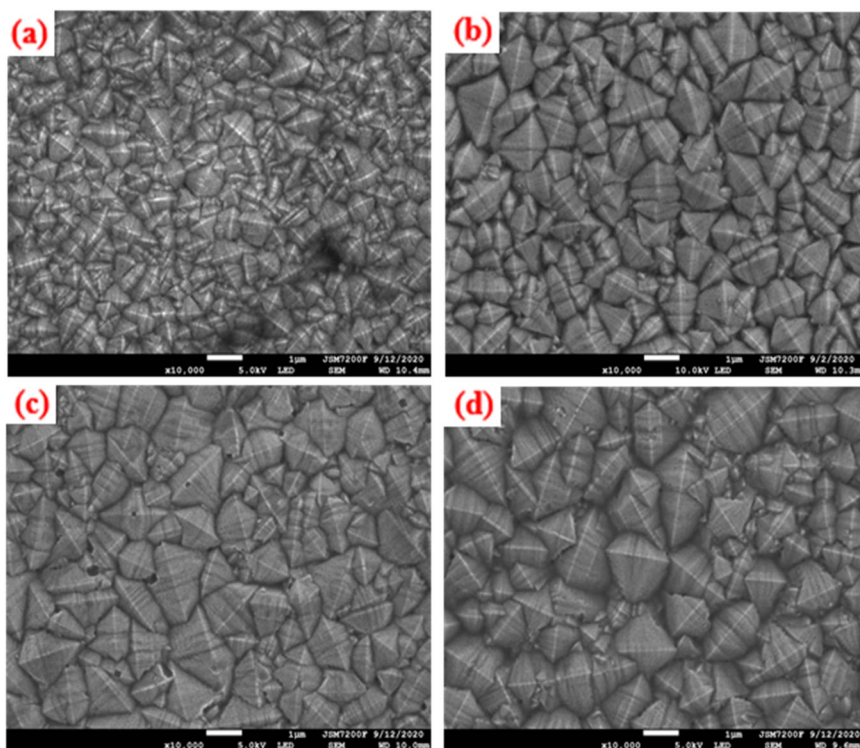


Fig. 7 SEM images of pure Ni coatings at different current densities. SEM images at current densities of (a) 1 A dm^{-2} , (b) 7 A dm^{-2} , (c) 9 A dm^{-2} , (d) $7 + 15 \text{ A dm}^{-2}$.

hydrophilic to hydrophobic. When the current density continued to increase to 9 A dm^{-2} the WCA began to drop to about 85° and the SA was slightly increased. When the secondary electrodeposition was adopted, the WCA of the obtained coatings was the largest, reaching about 95° , and the SA was reduced to less than 30° , which proved that the method of secondary electrodeposition was beneficial to improving the hydrophobicity of the Ni coatings.

Figure 7 shows the SEM images of the Ni coatings under different current densities. On the whole, the microscopic morphology of the pure nickel coatings exhibited sharp cone-like structure. As shown in Fig. 7a, when the current density was only 1 A dm^{-2} , the arrangement of the sharp cone structure was disorderly, and the height difference between the top “peak” and the lowest “valley” of the sharp cone was not obvious. It was difficult for such a structure to trap air to form an “air cushion”,

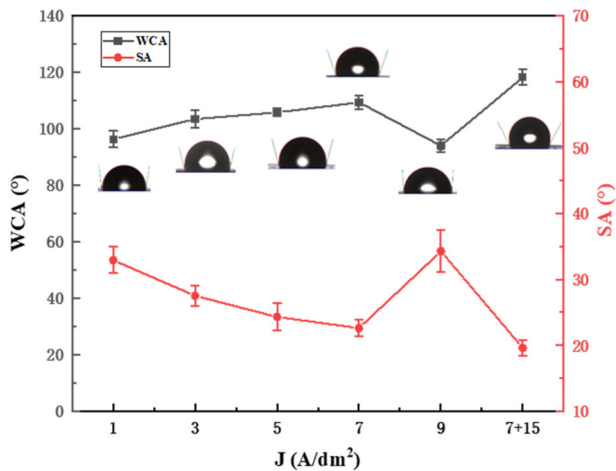


Fig. 8 WCA and SA of Ni-PTFE-SiC coatings at different current densities. The error bars indicate standard deviations.

and according to the results of MD simulations, metallic nickel itself had strong hydrophilicity, so the prepared coating had poor hydrophobicity at low current density. At 7 A dm^{-2} , it can be seen from Fig. 7b that micron sharp conical nickel crystals were closely arranged and a small number of nanoscale nickel crystals were scatteredly attached to micron nickel cones, so the WCA of the coating increased to more than 90° . When the current density continued to increase to 9 A dm^{-2} , due to the further increase of the driving force of the cathodic reaction, the cathodic over-potential increased. In the case of long electrodeposition time, the cathode surface lacked sufficient discharge metal ions, which led to obvious hydrogen evolution reaction, so a large number of porosity defects appeared on the conical structure of the coating as shown in Fig. 7c, which was also the reason for the decrease of the WCA. Figure 7d depicts that a large number of smaller (nanoscale) nickel grains were attached to the larger (micron-scale) sharp cones under secondary electrodeposition, which was due to the grain refinement effect of high current density^{37,38}. The micro-nano dual-scale surface structure further enhanced the hydrophobicity of the coating.

Figures 8, 9 show the wettability and SEM images of Ni-PTFE-SiC composite coatings at different current densities, respectively, when the content of both particles in the bath was 10 g L^{-1} . The sum of the weight percentage of F and Si elements obtained by EDS test is also shown in Fig. 9, which can be used to indirectly estimate the composite amount of PTFE and SiC nanoparticles. Obviously, compared with the pure nickel coatings, the hydrophobicity of the composite coatings had been significantly improved after adding two kinds of nanoparticles, with the maximum WCA reaching close to 120° and the SA lowering to less than 20° . It is found from Fig. 9a that only a small amount of particles were included in the coating at low current density, and the weight percentage of F and Si was only 2.1%. Nanoparticles wrapped by metal cations or surfactants^{37,39} need stronger driving force than Ni^{2+} to achieve the same migration speed during the electrodeposition process⁴⁰. Therefore, in comparison, more Ni ions were reduced and fewer particles were co-deposited at lower

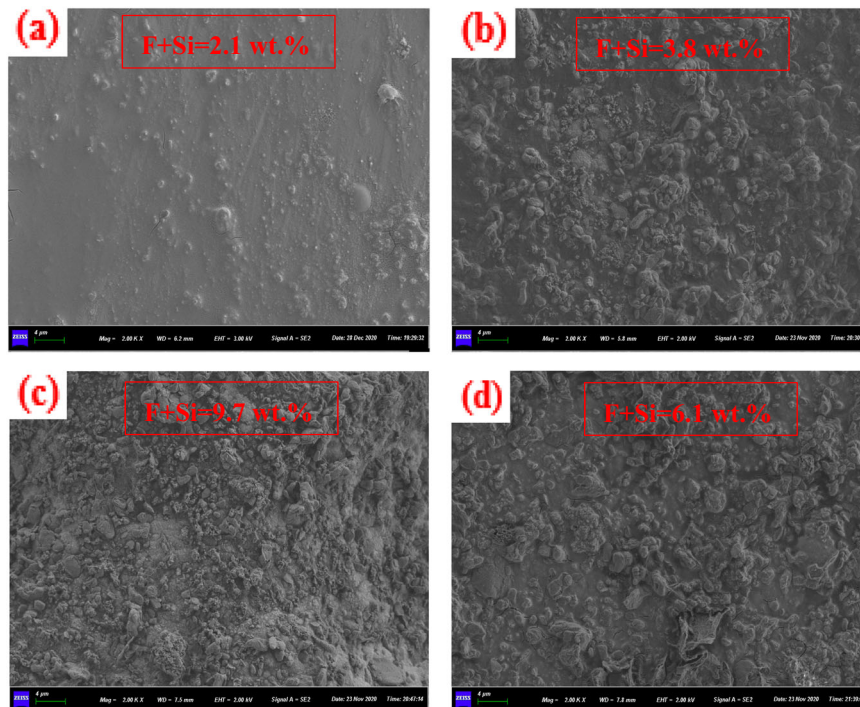


Fig. 9 SEM images of Ni-PTFE-SiC coatings at different current densities. SEM images at current densities of (a) 3 A dm^{-2} , (b) 7 A dm^{-2} , (c) 9 A dm^{-2} , (d) $7 + 15 \text{ A dm}^{-2}$.

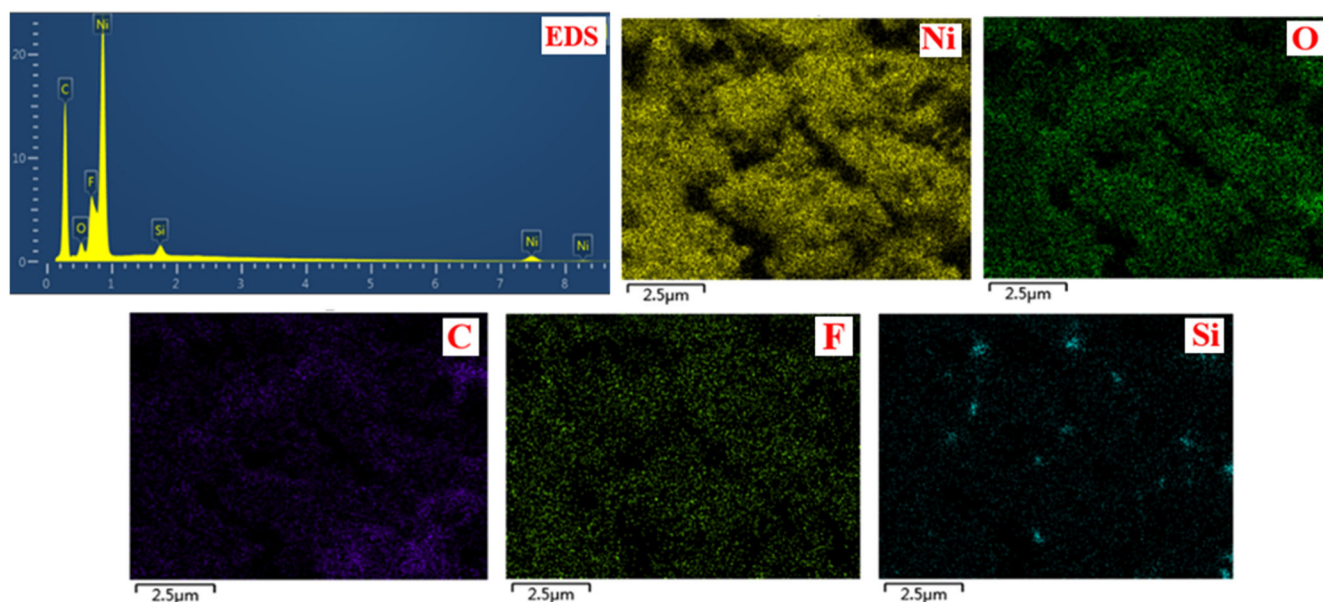


Fig. 10 Distribution of elements on the surface of the Ni-PTFE-SiC coatings.

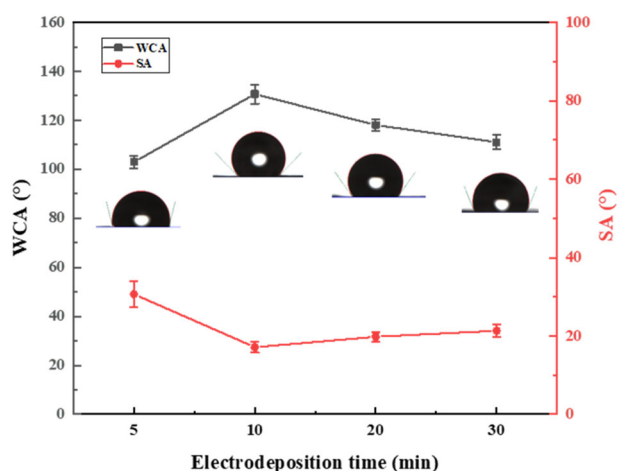


Fig. 11 WCA and SA of Ni-PTFE-SiC coatings at different electrodeposition time. The error bars indicate standard deviations.

current densities due to insufficient driving force. As the current density increased, the amount of inclusions of nanoparticles in the coating increased, as shown in Fig. 9b, the content of F and Si increased to 3.8% and the hydrophobicity also gradually increased. However, when the current density reached 9 A dm^{-2} , although the content of F and Si elements increased sharply to 9.7%, the hydrophobicity of the coating decreased slightly. As the current density increased, the electrostatic gravitation between the cathode and Ni^{2+} increased and the reduction rate of Ni^{2+} became faster, enhancing the ability of metal ions to “capture” nanoparticles^{41,42}. Coupled with enough deposition time (20 min), a large number of nanoparticles were deposited, eventually leading to irregular agglomeration of particles on the surface of the composite coating, as shown in Fig. 9c, which made the hydrophobicity of the coating slightly reduced. Compared with one-step electrodeposition, the hydrophobicity of the coating was the strongest under the secondary electrodeposition, indicating that the composite amount of nanoparticles in the coating under secondary electrodeposition was the most reasonable. At this time, the weight percentage of the F and Si elements in the coating was 6.1%, and since the high current density lasted only

5 min, the nanoparticles were not able to agglomerate in large quantities, as shown in Fig. 9d.

Figure 10 shows the distribution of elements in the composite coatings. The peak value of Ni element in EDS diagram was the highest, indicating that nickel was still the main component of the composite coatings. A trace amount of O element was detected, which came from the partial oxidation of metallic nickel. F element and Si element were detected, which proved that SiC and PTFE nanoparticles were successfully embedded in nickel matrix.

Figure 11 illustrates the WCA and SA of samples under different primary electrodeposition time at 7 A dm^{-2} , with the secondary electrodeposition time remaining constant at 15 A dm^{-2} for 5 min, and both PTFE and SiC particle contents were 10 g L^{-1} . When the first electrodeposition time was 5 min, the WCA of the coating was only about 100° and the SA was above 30° . When the electrodeposition time was increased to 10 min, the WCA of the coating suddenly increased to 130° and the SA dropped to less than 20° , meaning that the hydrophobic performance of the coating had been greatly improved. However, as the primary electrodeposition time continued to increase, the hydrophobicity of the coating began to decrease, especially when the primary electrodeposition time reached 30 min, the WCA of the coating decreased to 110° , and the SA increased to more than 20° .

Figure 12 reveals the micromorphology of the composite coatings at different electrodeposition time. When the deposition time was short, the nanoparticles didn't have enough time to be embedded in the coating, so the hydrophobicity of the coating was poor at this time. When the electrodeposition time was increased to 10 min, there had been already a large number of nanoparticles in the composite coating, and the particles of different scales were dispersed with each other and evenly distributed in the nickel-based metal, as shown in Fig. 12a, so that the hydrophobicity of the coating had been greatly improved. However, the continuous increase of deposition time would lead to the agglomeration of particles. As shown in Fig. 12b, when the electrodeposition time reached 30 min, the agglomeration of nanoparticles had become very serious. It can be observed that a large number of particles gathered together to form pieces of aggregates, which absorbed on the surface of the coating, resulting in the further weakening of the hydrophobic performance of the composite coatings.

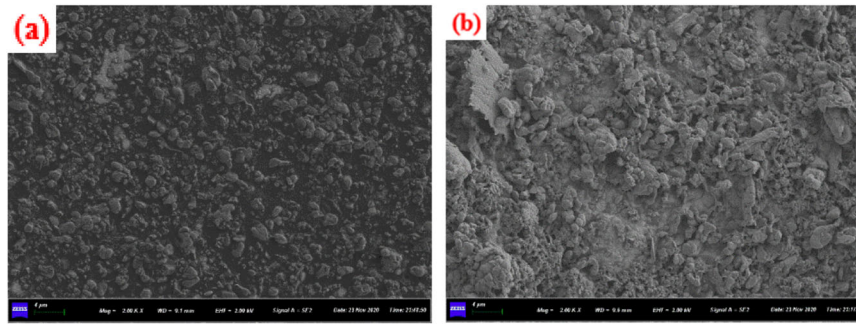


Fig. 12 SEM images of Ni-PTFE-SiC coatings at different electrodeposition time. SEM images at electrodeposition time of (a) 10 min, (b) 30 min.

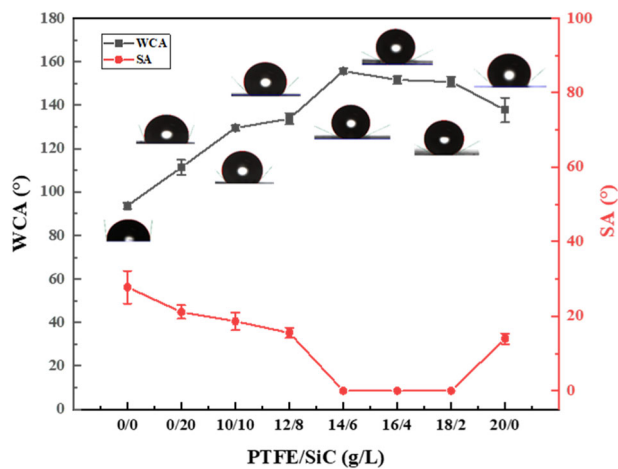


Fig. 13 WCA and SA of Ni-PTFE-SiC coatings at different concentrations of nanoparticles. The error bars indicate standard deviations.

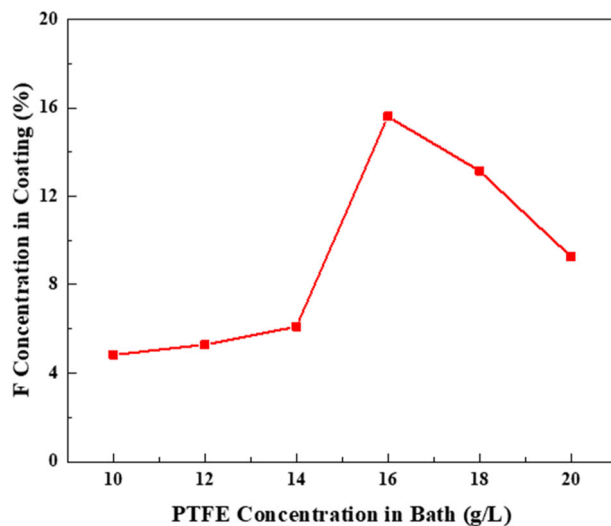


Fig. 14 The content of F element in the coatings at different PTFE concentrations in bath.

The WCA and SA of the Ni-PTFE-SiC coatings under different nanoparticle concentrations are shown in Fig. 13. It can be found that, when two types of nanoparticles were not added to the bath (0/0), the WCA of the coating was only slightly greater than 90°, and the SA was greater than 30°. Both SiC and PTFE nanoparticles

could improve the hydrophobicity of the coatings, especially the content of PTFE played a decisive role in the wettability of the coatings. As the concentration of PTFE increased, the hydrophobicity gradually enhanced. When the PTFE concentration was greater than 14 g L⁻¹ (14/6), the coating surface reached superhydrophobic state with the WCA more than 155°. When the droplet touched the surface of the coating, it would bounce immediately, that is, the SA was close to 0°. After that, when the concentration of PTFE particles was further increased to 16 g L⁻¹ (16/4) and 18 g L⁻¹ (18/2), the hydrophobicity of the coating surface remained relatively stable. But when the concentration of PTFE particles in the plating solution increased to 20 g L⁻¹ (20/0), the WCA dropped below 140°, and the SA increased to about 15°.

The wettability was actually determined by the composite amount and distribution of PTFE nanoparticles in the coatings. Figure 14 shows the variation of the weight percentage of element F in the coatings with the concentration of PTFE particles in the bath. With the increase of the PTFE concentration in the plating bath, the content of F element in the coatings showed an upward trend first, reaching a maximum of 15.61%, and then the content of F element decreased on the contrary. The reason for the decrease in the amount of F element embedded is that, on the one hand, the concentration of PTFE nanoparticles in the bath was too large, and agglomeration occurred, so large aggregates were difficult to move to the surface of the cathode. On the other hand, due to the good insulation of PTFE, the conductivity of the bath became worse with the increase of PTFE concentration, and the cathodic overpotential decreased, which led to hydrogen evolution reaction. This side reaction would affect the co-deposition of metals and nanoparticles⁴³. In addition, this phenomenon may also be caused by saturation adsorption effect⁴⁴, that is, when the concentration of nanoparticles in the bath reached a critical value, the adsorption capacity of nanoparticles on the cathode surface would reach saturation, so the composite amount of nanoparticles in the coatings cannot continue to increase.

Figure 15 shows the distribution of F element in the coatings under different PTFE nanoparticle concentrations in bath. It can be seen from Fig. 15a that when the concentration of PTFE nanoparticles in the bath was 14 g L⁻¹, the particles in the coating were dispersed with each other without agglomeration. When the concentration of PTFE nanoparticles in the plating solution increased to 16 g L⁻¹, as shown in Fig. 15b, although the F element content in the coating increased significantly (15.61%), it gathered together in pieces. This agglomeration weakened the hydrophobic effect of PTFE slightly. Therefore, in order to achieve the strongest hydrophobicity of the composite coatings, two conditions must be met, one is that there is sufficient content of PTFE in the coatings, and the other is the uniform distribution of nanoparticles in the coatings.

Figure 16 shows the SEM images of the composite coating when it reached the most superhydrophobic state (PTFE/SiC = 14/6 g L⁻¹). As shown in Fig. 16a, the two nanoparticles embedded in

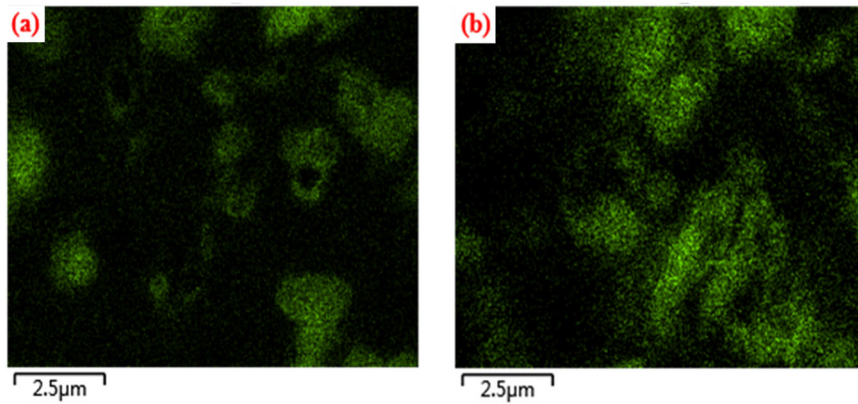


Fig. 15 The distribution of element F in the coatings under different PTFE nanoparticle concentrations in bath. The distribution of element F under the concentration of PTFE nanoparticles was (a) 14 g L^{-1} , (b) 16 g L^{-1} .

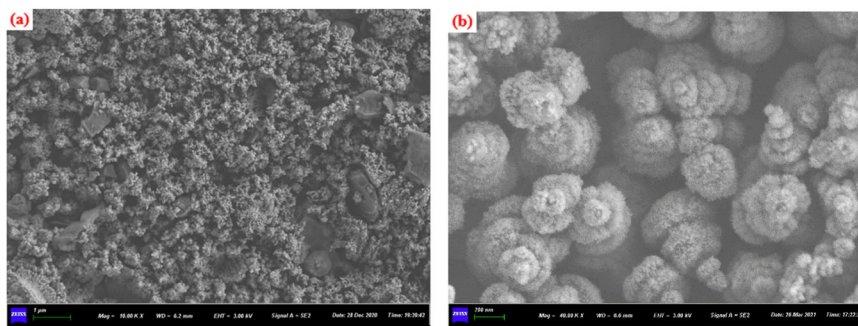


Fig. 16 SEM images of superhydrophobic Ni-PTFE-SiC coatings (PTFE/SiC = $14/6 \text{ g L}^{-1}$) with different magnifications. SEM images with magnification of (a) $\times 10,000$, (b) $\times 40,000$.

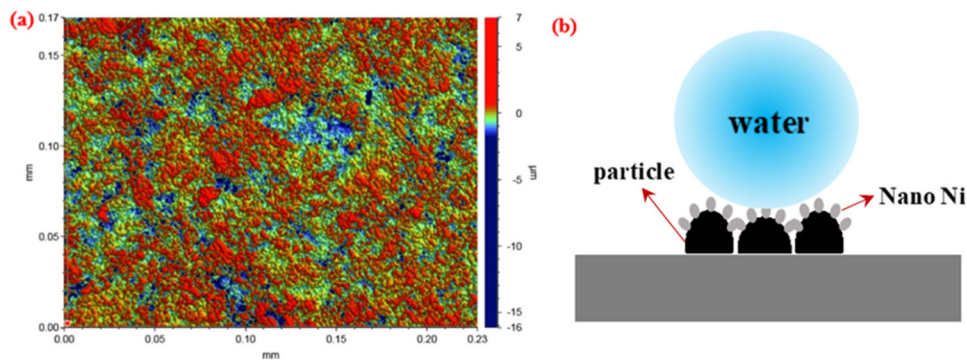


Fig. 17 3D topography of the superhydrophobic coating and schematic diagram of water droplets on the coating. **a** 3D topography of superhydrophobic coatings, **(b)** Schematic diagram of water droplets on micro-nano hierarchical structure.

the coating provided adsorption sites for the crystallization and growth of metallic nickel. Especially under the condition of secondary high current deposition, nickel atoms were rapidly grafted on the particles with very fine crystals, forming micro-nano dual-scale structure. In Fig. 16b, a number of micro-pores were observed on the surface with such structure. These pores could trap air to form an air cushion, preventing water droplets from penetrating into the surface, as illustrated in Fig. 17b, thus greatly improving the hydrophobicity of the coating. Figure 17a shows the 3D morphology of the coating, consistent with Fig. 16a. The surface of the coating was obviously distributed with protrusions of different sizes, which were two kinds of particles embedded in the coating, and the average roughness R_a of the coating surface was tested to be $0.47 \mu\text{m}$.

The current density, electrodeposition time and the concentration of nanoparticles in the bath affected the hydrophobicity by influencing the composite amount, distribution state of nanoparticles and morphology of coatings. When the concentrations of PTFE and SiC nanoparticles in the bath were 14 g L^{-1} and 6 g L^{-1} respectively, the current density of 7 A dm^{-2} was used for primary electrodeposition for 10 min, and then the current density of 15 A dm^{-2} was used for secondary electrodeposition for 5 min. At this time, the nanoparticles were uniformly distributed in the coating, and the coating was superhydrophobic with the WCA of more than 155° .

Figure 18 shows the polarization curves of bare substrate, ordinary Ni coating and the most superhydrophobic Ni-PTFE-SiC coating (SH coating) after soaking in corrosion medium for 0.5 h.

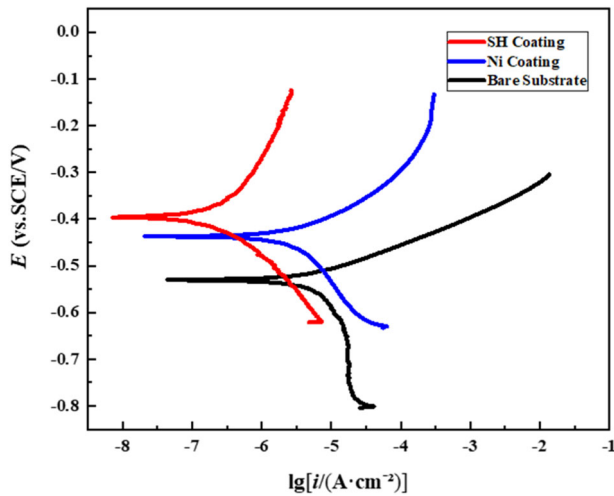


Fig. 18 Polarization curves of bare substrate, Ni coating and superhydrophobic coating.

Table 2. Data fitted according to polarization curves.			
Samples	E_{corr}/mV	$i_{corr}/A\cdot cm^{-2}$	η
Bare Substrate	-530.0	8.580×10^{-6}	—
Ni Coating	-436.7	4.891×10^{-6}	43.0%
SH Coating	-396.0	4.348×10^{-7}	95.0%

Based on this, the corrosion potential E_{corr} and corrosion current density i_{corr} of each sample were obtained by Tafel extrapolation and listed in Table 2. The anti-corrosion efficiency η of samples was calculated according to Eq. (4), where $i_{corr,sub}$ and $i_{corr,coated}$ respectively represent the corrosion current density of the bare substrate and the coated sample.

$$\eta = \frac{i_{corr,sub} - i_{corr,coated}}{i_{corr,sub}} \times 100\% \quad (4)$$

It can be found from Fig. 18 and Table 2 that compared with the bare carbon steel substrate, the E_{corr} of the sample with ordinary nickel coating was significantly positive and the i_{corr} was slightly reduced, indicating that the ordinary Ni coating could enhance the corrosion resistance of the substrate, but the calculated anti-corrosion efficiency η was only about 43.0%. In contrast, the E_{corr} of sample with superhydrophobic Ni-PTFE-SiC composite coating was the most positive, and the i_{corr} was only approximately 1/20 of bare substrate and 1/11 of Ni coating. The anti-corrosion efficiency of superhydrophobic Ni-PTFE-SiC composite coating was as high as 95.0%, which indicated that the superhydrophobic coating had excellent protection effect.

The Nyquist plots of different samples after soaking in corrosion medium for 0.5 h are shown in Fig. 19. Clearly, the capacitive arc radius of the sample with the superhydrophobic coating was significantly larger than that of the bare carbon steel substrate and the nickel coating, a symbol of the excellent anti-corrosion effect.

The equivalent circuits shown in Fig. 20 were used to fit the EIS data and the fitting data are shown in Table 3. R_s , R_c and R_{ct} are solution resistance, coating resistance and charge transfer resistance respectively. CPE_{dl} and CPE_c are constant phase angle elements to simulate the capacitance at the interface of solution/substrate and solution/coating⁴⁵. Considering the roughness and energy dissipation of the electrode surface³², the constant phase angle element is often used to replace the ideal capacitance, and

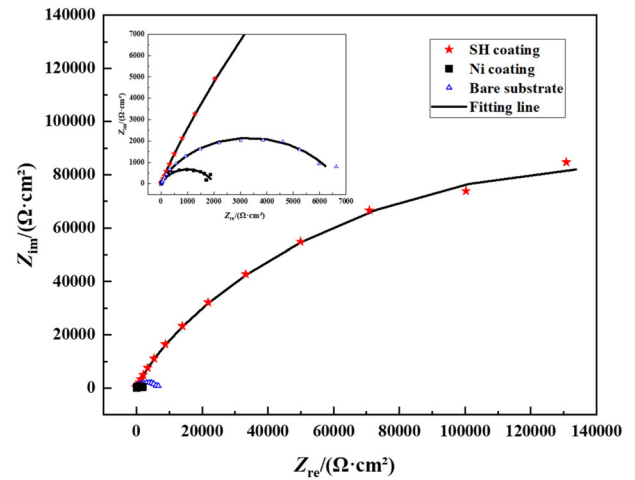


Fig. 19 Nyquist plots of bare substrate, Ni coating and superhydrophobic coating.

its impedance is defined by Eq. (5):

$$Z_{CPE} = \frac{1}{Y_0} (j\omega)^{-n} \quad (5)$$

In the formula, Y_0 is a constant, $s^n \Omega^{-1} cm^{-2}$, ω is the angular frequency, $rad s^{-1}$. j is an imaginary number and n is a dispersion index.

Table 3 reveals the internal mechanism of the excellent anti-corrosion effect of superhydrophobic coatings. First of all, the film resistance R_c of the ordinary Ni coating itself was only $51 \Omega\cdot cm^2$, while the R_c of the superhydrophobic composite coating reached $1.289 \times 10^3 \Omega\cdot cm^2$. The reason was that the coating was embedded with chemically inert SiC and PTFE nanoparticles, thus enhancing the corrosion resistance of the coating itself. On the other hand, the R_{ct} of bare carbon steel substrate and Ni coating was only $1.989 \times 10^3 \Omega\cdot cm^2$ and $6.740 \times 10^3 \Omega\cdot cm^2$, respectively, while the R_{ct} of the superhydrophobic composite coating was as high as $3.088 \times 10^5 \Omega\cdot cm^2$, which was two orders of magnitude higher than that of the nickel coating. The significant increase of R_{ct} indicated that the strong water repellent capacity of the superhydrophobic surface hindered the penetration of the corrosion medium into the coating and contact with the substrate, which greatly increased the resistance of the corrosion reaction and dramatically improved the anti-corrosion effect of the coating.

To compare the wear resistance of the composite coatings, the modified superhydrophobic coatings were prepared by soaking the ordinary nickel coatings in myristic acid, and Fig. 21 shows the WCA and SA of two kinds of superhydrophobic coatings at different wear distances. From Fig. 21a, it can be found that after modification with myristic acid, the nickel coating presented superhydrophobic state with the WCA up to 156° and the SA of 0° . After only 120 cm of abrasion, the WCA of the coating had dropped to 150° and the SA had increased to 4° . When the wear distance reached 160 cm, the WCA decreased sharply to less than 140° and the SA increased to more than 10° , which meant that the hydrophobicity of the coating began to decrease sharply. When the wear distance reached 400 cm, the WCA and SA became less than 120° and nearly 20° respectively, so it was difficult to maintain good hydrophobicity for modified coatings.

In contrast, it can be seen from Fig. 21b that for the Ni-PTFE-SiC composite coating, the WCA was still more than 150° and the SA was less than 5° until the wear distance reached 200 cm, that is to say, the coating was still superhydrophobic. When the wear distance exceeded 280 cm, although the hydrophobicity of the coating continued to decline, the rate of decrease became

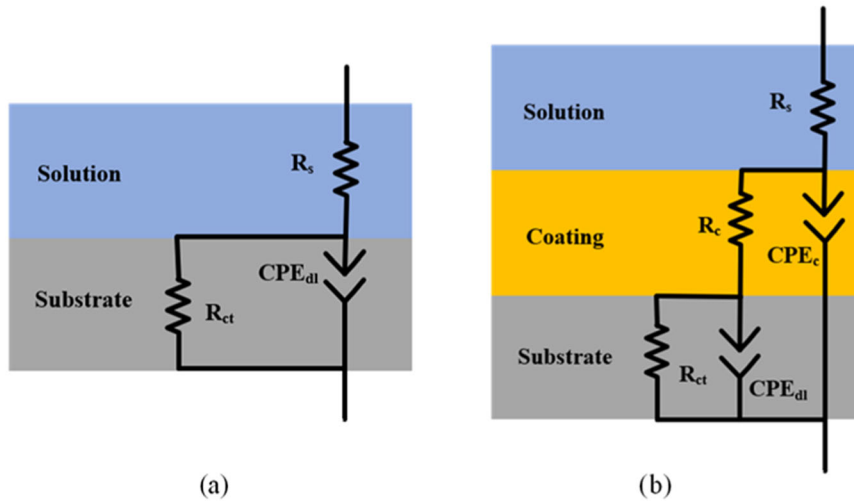


Fig. 20 Equivalent circuit diagrams for impedance spectrum fitting. Equivalent circuit diagrams applicable to (a) bare substrate, (b) coated samples.

Samples	$R_s/\Omega \text{ cm}^2$	CPE _{dl}		$R_{ct}/\Omega \text{ cm}^2$	CPE _c		$R_c/\Omega \text{ cm}^2$
		$Y_0/s^n \Omega^{-1} \text{ cm}^{-2}$	n_1		$Y_0/s^n \Omega^{-1} \text{ cm}^{-2}$	n_2	
Bare Substrate	5.6	5.383×10^{-4}	0.759	1.989×10^3	—	—	—
Ni Coating	5.9	1.360×10^{-4}	0.664	6.740×10^3	3.766×10^{-5}	0.933	51
SH Coating	5.9	2.080×10^{-6}	0.843	3.231×10^5	3.846×10^{-6}	0.506	1.289×10^3

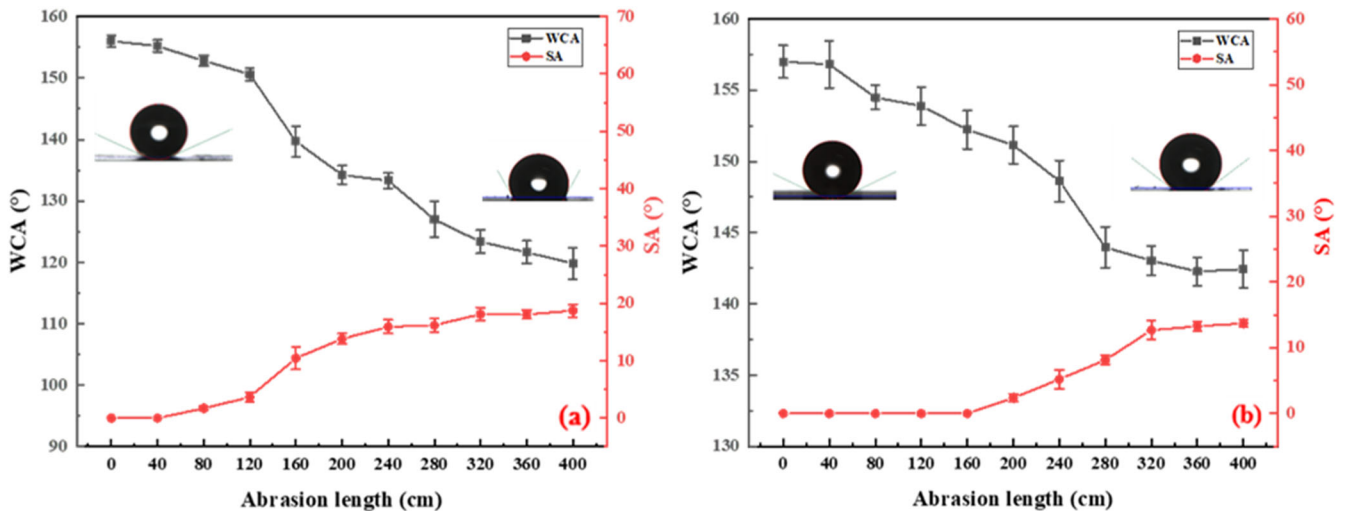


Fig. 21 WCA and SA of samples under different wear distances. WCA and SA of (a) modified coatings, (b) Ni-PTFE-SiC composite coatings. The error bars indicate standard deviations.

relatively slow. The WCA of the coating remained above 142° and the SA was below 15° until the wear distance reached 360 cm. Then, the hydrophobicity of the coating changed little with increasing the wear distance. Therefore, compared with the modified coatings, the wear resistance of the composite coatings had been greatly improved.

Figure 22 depicts that the surface morphology of these two kinds of coatings after the sand abrasion experiment was greatly different. As shown in Fig. 22 (a) and (a-i), the wear marks on the surface of the modified coating were very obvious, wide, deep and

numerous in number due to the poor hardness and adhesion of a layer of modifier on the surface, which constantly fell off in the wear process, forming a large number of irregular wear marks and leading to the rapid deterioration of the hydrophobicity. However, very slight wear marks could be observed on only part of the surface of the composite coating, as shown in Fig. 22 (b) and (b-i). On the one hand, due to the high hardness of SiC, on the other hand, the self-lubricity of PTFE also reduced the friction coefficient of the coating, resulting in light wear of the composite coating. Moreover, because the two kinds of nanoparticles were

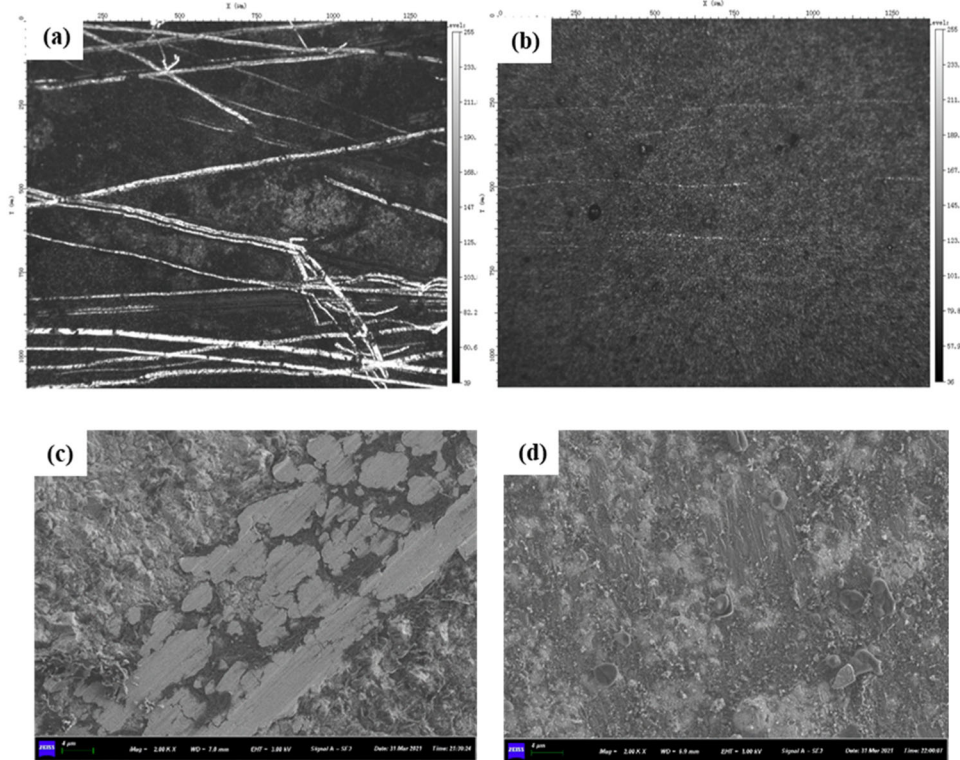


Fig. 22 Surface morphology of different samples after wear. Surface morphology of (a) modified coatings, (b) Ni-PTFE-SiC composite coatings, (c) and (d) are the corresponding SEM images.

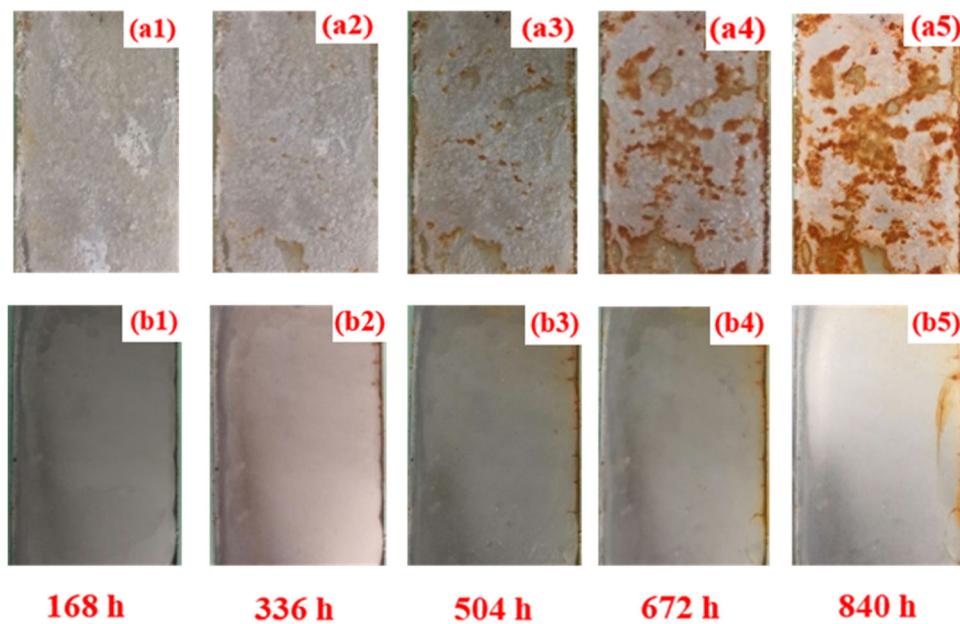


Fig. 23 Corrosion morphology of samples changing with immersion time. Surface morphology of (a) modified coatings, (b) Ni-PTFE-SiC composite coatings.

embedded in the coating, as the wear distance continued to increase, the nanoparticles were continuously exposed, so that the hydrophobicity of the coating kept relatively stable.

Figure 23 shows the corrosion morphology of the modified superhydrophobic coating and Ni-PTFE-SiC composite superhydrophobic coating immersed in 3.5 wt.% NaCl solution for 840 h. After 168 h of soaking, the surface morphology of both the two coatings hardly changed. But after 336 h, the difference began to

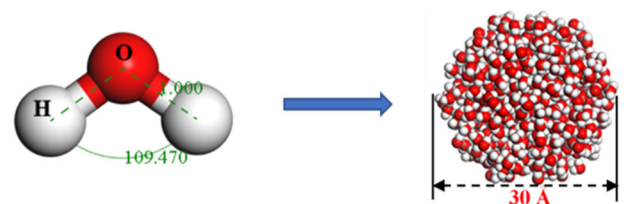


Fig. 24 Schematic diagram of water droplets model.

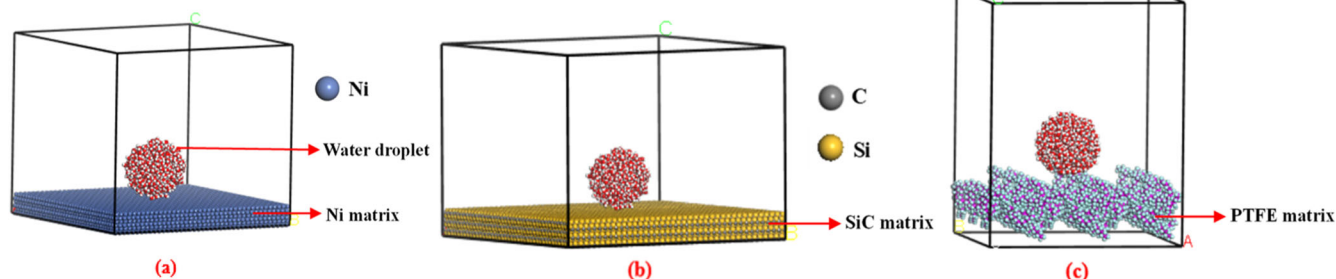


Fig. 25 Initial configuration of different matrix. Initial configuration of (a) water droplet-Ni matrix, (b) water droplet-SiC matrix, (c) water droplet-PTFE matrix.

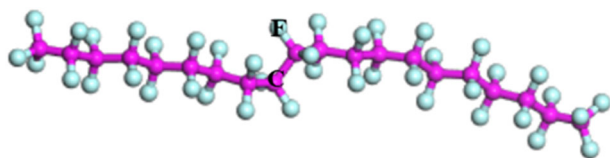


Fig. 26 PTFE molecular structure after geometry optimization.

show up. The corrosion of the composite superhydrophobic coating was very slight only in the weak area of the interface between the epoxy resin and the sample, while a layer of myristic acid molecules on the surface of the modified coating had visibly fallen off in the local area. When the immersion time continued to increase, the corrosion of the composite coating almost did not develop, while the peeling off of the modifier on the surface of the modified coating became more and more serious. The modifiers that originally fell off in spots were gradually connected into pieces, and large exposed areas developed into weak corroded areas. By contrast, the composite superhydrophobic coating obviously showed better durability. After immersing for 840 h, most areas still maintained good corrosion protection effect.

The anti-corrosion efficiency of Ni-PTFE-SiC superhydrophobic coatings reached 95%. They also had better wear resistance and durability compared with the modified coatings. Through MD simulations, the good stability of the Ni-PTFE-SiC composite coatings was due to the fact that SiC and PTFE nanoparticles moved to the substrate together under the tightly entrapment of Ni, forming metal bonds with the substrate. The composite film had strong adhesion, low diffusion coefficient and slow diffusibility, so that the composite coatings could be stably adsorbed on the substrate.

METHODS

Design of superhydrophobic coatings

In order to explore whether the addition of SiC and PTFE is beneficial to the improvement of the hydrophobicity of Ni-based coatings, we first simulated the wetting behavior of water droplets on the surface of these three different materials.

The commercially purchased software, Materials Studio (MS), was used to build initial configuration and run MD simulations. The SPC model⁴⁶ was chosen to describe the interactions between water molecules. Then, the Amorphous Cell module in the software was utilized to construct a cell composed of 1000 water molecules with a density of 1 g cm^{-3} , followed by the construction of spherical water droplets with a diameter of 30 \AA using Nanocluster build function, as shown in Fig. 24.

The Ni crystal cell structure was imported from the crystal library of MS with lattice parameters of $a = b = c = 3.524 \text{ \AA}$ and $\alpha = \beta = \gamma = 90^\circ$. After the geometry optimization of the cell structure by using the CASTEP module, the lattice parameters

were changed to $a = b = c = 3.547 \text{ \AA}$. Subsequently, the crystal cell was cut along the (1 0 0) plane⁴⁷ using the Cleave Surface tool and the Thickness was set to 3. Then, the crystal plane was expanded into a supercell with $U \times V = (40 \times 40)$, and the Build Vacuum Slab tool was used to add a vacuum layer with a thickness of 80 \AA on top of the supercell. At this time, a 3D cuboid box with the size of $(100.3 \times 100.3 \times 88.9) \text{ \AA}$ was constructed. Eventually, the droplet model shown in Fig. 1 was placed directly above the Ni matrix and the initial configuration of the droplet-Ni matrix was successfully established, as shown in Fig. 25a. Similarly, we constructed the initial model of water droplet-SiC matrix with a size of $(123.6 \times 123.6 \times 92.0) \text{ \AA}$ by the same method, as depicted in Fig. 25b.

Figure 26 shows the molecular structure of PTFE consisting of ten repeating units constructed by the Build Polymer function in MS. Based on this, the supercell composed of PTFE molecules was built followed by the addition of the vacuum layer and the placement of the water droplet, and then the droplet-PTFE matrix model with a size of $(90.0 \times 90.0 \times 89.2) \text{ \AA}$ was completed, as shown in Fig. 25c.

All the MD simulations were carried out by using the COMPASS force-field in the Forcite module of MS. It should be noted that geometry optimization by Smart algorithm³⁰ was required after each model was established to save subsequent simulation time. The canonical ensemble (NVT) was employed at 298 K for each simulation system and the temperature control was achieved by Andersen method⁴⁸. The electrostatic interaction was calculated by the Ewald method⁴⁹, while for van der Waals interaction, the atom-based method was applied with the cutoff distance set to 15.5 \AA .

Following this, the MD simulations lasted for 1000 ps in total with a time step of 1.0 fs . One frame of image was exported every 5000 steps, that is, a total of 201 frames of image were exported in the whole process of each simulation, and the convergence accuracy was set to Fine.

The stable adsorption of the coatings on the substrate is the key to improving durability. Therefore, we explored the interaction between the Ni-PTFE-SiC composite film and the substrate by MD simulations to find out whether it could be stably adsorbed. Since the traditional preparation process of superhydrophobic coatings requires surface modification with low surface energy substances, we also simulated the interaction between modifier molecules and the substrate for comparison.

Myristic acid, commonly used in the preparation of superhydrophobic coatings¹¹, was selected as modifier. The Amorphous Cell module was used to construct an amorphous cell containing 40 myristic acid molecules with a density of 0.862 g cm^{-3} . Then, a double-layer structure with Ni as the first layer and myristic acid amorphous cell as the second layer was constructed by Build Layer function, and a 50 \AA vacuum layer was added at the top. In this way, a simulation system of myristic acid-Ni superhydrophobic coatings had been constructed, as shown in Fig. 27a.

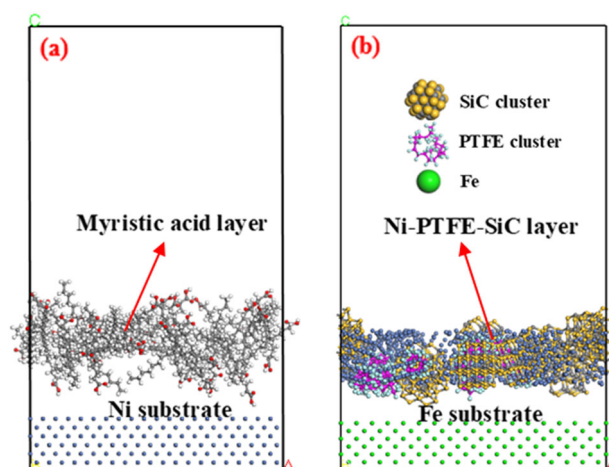


Fig. 27 Initial configuration of different matrix. Initial configuration of (a) myristic acid film-Ni matrix and (b) Ni-PTFE-SiC film-Fe matrix.

Similarly, the amorphous cell with 10 SiC particles and 10 PTFE particles embedded in nickel atoms was constructed and placed on the Fe substrate which was used to replace the carbon steel matrix. Among them, SiC and PTFE particles were clusters with a diameter of 1 nm, drawn through the Nanocluster Build function in MS. After adding a 50 Å vacuum layer, the interaction system between Ni-PTFE-SiC composite film and Fe matrix was completed, as shown in Fig. 27b. The simulation details were set as described in section 2.1.2.

Fabrication of superhydrophobic coatings

A two-electrode system was used for the electrodeposition process, in which the cathode was ASME A106B steel substrates (50 mm × 25 mm × 2 mm) with the compositions (in wt.%): 0.19 C, 0.28Si, 0.52Mn, 0.25Cr, 0.3Ni, 0.25Cu, 0.035 P, 0.035 S and balance Fe. The anode was Ni plates (60 mm × 40 mm × 2 mm) with a purity of 99.96%. Only one side of the cathode plate was exposed and the other five surfaces were encapsulated with non-conductive epoxy resin, that is, the area to be plated was 12.5 cm². The exposed surface of the cathode was polished with 180, 400, 600, 800 and 1200 grit SiC sandpaper in turn and then ultrasonically cleaned in ethanol. During electrodeposition, the two electrodes were kept parallel to each other with a distance of 6 cm.

The chemical composition of the plating bath included 250 g L⁻¹ NiSO₄·6H₂O, 40 g L⁻¹ NiCl₂·6H₂O, 40 g L⁻¹ H₃BO₃ and 50 g L⁻¹ of NH₄Cl as crystal modifier³⁷. The contents of PTFE particles (0.7–0.9 μm) and SiC particles (0.5–0.7 μm) added into the bath were 0–20 g L⁻¹ and 0–10 g L⁻¹, respectively. In order to ensure the stable dispersion of nanoparticles in the bath, they were added to deionized water containing cationic surfactant cetyltrimethyl ammonium bromide (CTAB)⁵⁰ at a concentration of 0.05 g g⁻¹ particles, followed by ultrasonic dispersion of 30 min and high-speed magnetic stirring of 30 min. Once dispersed, the dispersion system was mixed with other components and the plating solution was prepared.

Before electrodeposition, the sample needed to be degreased with alkaline washing solution (12 g L⁻¹ NaOH, 60 g L⁻¹ Na₂CO₃ and 30 g L⁻¹ Na₂SiO₃·9H₂O) at 75 °C for 10 min and then activated with 10 wt.% HCl for 1 min at room temperature. The stable DC current was provided by a DC power supply. Electrodeposition process was carried out in a constant temperature water bath at 50 °C and the pH of the bath was maintained at about 4 with dilute sulfuric acid or ammonia, assisted by magnetic stirring at 1300 revolutions per minute to ensure the stable dispersion of nanoparticles and timely mass transfer. The applied current density was 1–9 A dm⁻² and the electrodeposition time was

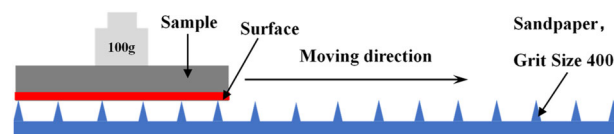


Fig. 28 Schematic diagram of sand abrasion experiment.

5–30 min. Further, some samples were subjected to secondary electrodeposition for 5 min at a current density of 15 A dm⁻². After the electrodeposition, the samples were ultrasonically cleaned in ethanol for 3 min, and then fully dried in air for subsequent characterization. Samples with a pure nickel coating without nanoparticles were immersed in molten myristic acid for 2 h at 60 °C, hereafter referred to as a “modified superhydrophobic coating”, as a comparison to test the performance of the composite coating.

The water contact angle (WCA) and sliding angle (SA) of the coating surface were measured by a fully automatic contact angle measuring instrument (SDC-350, SINDIN, China) to characterize the wettability of coatings. The volume of deionized water droplets used in the measurement of WCA and SA were 5 μL and 8 μL respectively, and the average value of five points on the surface was taken as the final results. The surface morphology of coatings was observed by field emission scanning electron microscope (SEM, GeminiSEM 300, ZEISS, Germany), which was equipped with energy dispersive X-ray spectroscopy (EDS) to analyze the chemical composition of coatings. White light interferometer (WLI, Contour GT, Bruker, Germany) was used to test the 3D topography of the coatings.

The corrosion resistance of coatings was characterized by electrochemical test⁵¹ using a potentiostat (PARSTAT 2273, Electrochem). A standard three-electrode system was adopted with the samples as working electrodes, a saturated calomel electrode and a platinum electrode as reference electrode and counter electrode, respectively. The corrosive medium was 3.5 wt.% NaCl solution, and the working area was 1 cm². Before the test, the sample was immersed in the solution for 0.5 h to reach a stable state. The frequency range of the electrochemical impedance spectroscopy (EIS) test was 10⁵–10⁻² Hz with a sinusoidal amplitude of 10 mV. Zsimpwin software was used to fit the EIS data. For the Tafel polarization curve test, the potential range was ±250 mV versus open circuit potential (OCP) with a scan rate of 0.5 mV s⁻¹, and the data was fitted with Power Suite software.

The wear resistance of samples was tested by self-made sand abrasion experiment^{25,52–55}. According to Fig. 28, the sample was put face-down to 400 grit SiC sandpaper with a 100 g weight placed above the sample. Then, the sample was dragged on the sandpaper at a constant speed of 1.6 cm s⁻¹ to measure the change of WCA and SA at different abrasion distances. To ensure the accuracy of the experiment, a motor that could rotate at a uniform speed was used to pull the rope, and then the rope would drag the sample at a uniform speed of 1.6 cm s⁻¹. The durability of coatings was characterized by observing the corrosion morphology of samples immersed in 3.5 wt.% NaCl solution for 840 h.

DATA AVAILABILITY

The data are available from the corresponding author on reasonable request.

Received: 1 July 2023; Accepted: 30 October 2023;

Published online: 17 November 2023

REFERENCES

- Saji, V. S. Recent progress in superhydrophobic and superamphiphobic coatings for magnesium and its alloys. *J. Magnes. Alloy* **9**, 748–778 (2021).

2. Fihri, A., Bovero, E., Al-Shahrani, E. A., Al-Ghamdi, A. & Alabedi, G. Recent progress in superhydrophobic coatings used for steel protection: a review. *Colloids Surf. Physicochem. Eng. Aspects* **520**, 378–390 (2017).
3. Yao, W. et al. Superhydrophobic coatings for corrosion protection of magnesium alloys. *J. Mater. Sci. Technol.* **52**, 100–118 (2020).
4. Zhang, B., Duan, J., Huang, Y. & Hou, B. Double layered superhydrophobic PDMS-Candle soot coating with durable corrosion resistance and thermal-mechanical robustness. *J. Mater. Sci. Technol.* **71**, 1–11 (2021).
5. Usman, J. et al. An overview of superhydrophobic ceramic membrane surface modification for oil-water separation. *J. Mater. Res. Technol.* **12**, 643–667 (2021).
6. Lin, Y. et al. Superhydrophobic photothermal coatings based on candle soot for prevention of biofilm formation. *J. Mater. Sci. Technol.* **132**, 18–26 (2023).
7. Li, W., Zhan, Y. & Yu, S. Applications of superhydrophobic coatings in anti-icing: theory, mechanisms, impact factors, challenges and perspectives. *Prog. Org. Coat.* **152**, 106117 (2021).
8. Varshney, P. & Mohapatra, S. S. Durable and regenerable superhydrophobic coatings for brass surfaces with excellent self-cleaning and anti-fogging properties prepared by immersion technique. *Tribol. Int.* **123**, 17–25 (2018).
9. Saji, V. S. Wax-based artificial superhydrophobic surfaces and coatings. *Colloids Surf. Physicochem. Eng. Aspects* **602**, 125132 (2020).
10. Wang, D. et al. Design of robust superhydrophobic surfaces. *Nature* **582**, 55–59 (2020).
11. Xiang, T. et al. Robust superhydrophobic coating with superior corrosion resistance. *J. Alloys Compd.* **798**, 320–325 (2019).
12. Shen, L., Fan, M., Qiu, M., Jiang, W. & Wang, Z. Superhydrophobic nickel coating fabricated by scanning electrodeposition. *Appl. Surf. Sci.* **483**, 706–712 (2019).
13. Zhou, N., Wang, S. & Walsh, F. C. Effective particle dispersion via high-shear mixing of the electrolyte for electroplating a nickel-molybdenum disulphide composite. *Electrochim. Acta* **283**, 568–577 (2018).
14. Wang, M. et al. Achieving high ductility in layered carbon nanotube/copper composite prepared by composite electrodeposition. *Diamond Relat. Mater.* **108**, 107992 (2020).
15. Zhou, J. et al. Electroplating of non-fluorinated superhydrophobic Ni/WC/WS₂ composite coatings with high abrasive resistance. *Appl. Surf. Sci.* **487**, 1329–1340 (2019).
16. Zhang, H. et al. Ni–SiC composite coatings with improved wear and corrosion resistance synthesized via ultrasonic electrodeposition. *Ceram. Int.* **47**, 9437–9446 (2021).
17. Zhou, Y. et al. Tribological behavior of Ni–SiC composite coatings produced by circulating-solution electrodeposition technique. *Tribol. Int.* **159**, 106933 (2021).
18. Ji, R. et al. Preparation of Ni–SiC nano-composite coating by rotating magnetic field-assisted electrodeposition. *J. Manuf. Process.* **57**, 787–797 (2020).
19. Jiang, W., Shen, L., Xu, M., Wang, Z. & Tian, Z. Mechanical properties and corrosion resistance of Ni-Co-SiC composite coatings by magnetic field-induced jet electrodeposition. *J. Alloys Compd.* **791**, 847–855 (2019).
20. Wasekar, N. P., Latha, S. M., Ramakrishna, M., Rao, D. S. & Sundararajan, G. Pulsed electrodeposition and mechanical properties of Ni-W/SiC nano-composite coatings. *Mater. Des.* **112**, 140–150 (2016).
21. Jiang, W. et al. Multi-physics coupled deposition of Ni-PTFE-SiC composite coating and investigation of its properties. *Surf. Topogr.-Metrol.* **8**, 025005 (2020).
22. Wu, Y., Liu, L., Shen, B. & Hu, W. Study of self-lubricant Ni-P-PTFE-SiC composite coating. *J. Mater. Sci.* **40**, 5057–5059 (2005).
23. Huang, Y. S., Zeng, X. T., Annergren, I. & Liu, F. M. Development of electroless NiP-PTFE-SiC composite coating. *Surf. Coat. Tech.* **167**, 207–211 (2003).
24. Iacovetta, D., Tam, J. & Erb, U. Synthesis, structure, and properties of superhydrophobic nickel-PTFE nanocomposite coatings made by electrodeposition. *Surf. Coat. Tech.* **279**, 134–141 (2015).
25. Tam, J., Jiao, Z., Lau, J. C. F. & Erb, U. Wear stability of superhydrophobic nano Ni-PTFE electrodeposits. *Wear* **374–375**, 1–4 (2017).
26. Tam, J., Lau, J. C. F. & Erb, U. Thermally robust non-wetting Ni-PTFE electrodeposited nanocomposite. *Nanomaterials* **9**, 1–11 (2018).
27. Ibe, T., Kiyokawa, H., Chong, Y. B., Yonezawa, S. & Takashima, M. Electrodeposition and surface properties of nickel-PTFE composite film. *J. Soc. Mater. Sci.* **47**, 148–152 (1998).
28. Wang, F., Arai, S. & Endo, M. Electrochemical preparation and characterization of nickel/ultra-dispersed PTFE composite films from aqueous solution. *Mater. Trans.* **45**, 1311–1316 (2004).
29. Hao, Q., Ming, P. & Cui, T. Preparation of super-hydrophobic Ni-PTFE composite coatings using electrophoretic-electrochemical deposition process. *Electromach. Mould.* **49**, 29–32 (2014).
30. Sethi, S. K., Soni, L., Shankar, U., Chauhan, R. P. & Manik, G. A molecular dynamics simulation study to investigate poly(vinyl acetate)-poly(dimethyl siloxane) based easy-clean coating: an insight into the surface behavior and substrate interaction. *J. Mol. Struct.* **1202**, 127342 (2020).
31. Kitabata, M., Taddese, T. & Okazaki, S. Molecular dynamics study on wettability of poly(vinylidene fluoride) (PVDF) crystalline and amorphous surfaces. *Langmuir* **34**, 12214–12223 (2018).
32. Liu, J. et al. Synergistic inhibition effect of imidazoline and thiourea: evidence from experiments and molecular dynamics simulation. *Corrosion* **76**, 1194–1206 (2020).
33. Guo, J., Zhang, L., Liu, S. & Li, B. Effects of hydrophilic groups of nonionic surfactants on the wettability of lignite surface: molecular dynamics simulation and experimental study. *Fuel* **231**, 449–457 (2018).
34. Kornherr, A. et al. Adsorption of organosilanes at a Zn-Terminated ZnO (0001) surface: molecular dynamics study. *Langmuir* **22**, 8036–8042 (2006).
35. Hu, S. Q. et al. Computer simulation of diffusion of corrosive particle in corrosion inhibitor membrane. *Comput. Theor. Chem.* **964**, 176–181 (2011).
36. Garrido, L., Pozuelo, J., López-González, M., Fang, J. & Riande, E. Simulation and experimental studies on proton diffusion in polyelectrolytes based on sulfonated naphthalenic copolyimides. *Macromolecules* **42**, 6572–6580 (2009).
37. Liu, J. et al. Fabrication of superhydrophobic coatings for corrosion protection by electrodeposition: a comprehensive review. *Colloids Surf. Physicochem. Eng. Aspects* **607**, 125498 (2020).
38. Li, H., Yu, S., Han, X., Zhang, S. & Zhao, Y. A simple method for fabrication of bionic superhydrophobic zinc coating with crater-like structures on steel substrate. *J. Eng. Technol.* **13**, 622–630 (2016).
39. Celis, J. P., Roos, J. & Buelens, C. A mathematical model for the electrolytic co-deposition of particles with a metallic matrix. *J. Electrochem. Soc.* **134**, 1402–1408 (1987).
40. Guo, C., Zuo, Y., Zhao, X., Zhao, J. & Xiong, J. The effects of electrodeposition current density on properties of Ni-CNTs composite coatings. *Surf. Coat. Tech.* **202**, 3246–3250 (2008).
41. Wang, Y. & Zhang, L. Preparation and numerical simulation of Ni-SiC composite coatings deposited by electrodeposition. *Appl. Mech. Mater.* **543–547**, 3707–3710 (2014).
42. Alipour, K. & Nasirpour, F. Effect of morphology and surface modification of silica nanoparticles on the electrodeposition and corrosion behavior of Zinc-based nanocomposite coatings. *J. Electrochem. Soc.* **166**, D1–D9 (2019).
43. He, Y. et al. The monitoring of coating health by in situ luminescent layers. *RSC Adv.* **5**, 42965–42970 (2015).
44. Guglielmi, N. Kinetics of the deposition of inert particles from electrolytic baths. *J. Electrochem. Soc.* **119**, 1009–1012 (1972).
45. Jiang, D., Zhou, H., Wan, S., Cai, G. Y. & Dong, Z. H. Fabrication of superhydrophobic coating on magnesium alloy with improved corrosion resistance by combining micro-arc oxidation and cyclic assembly. *Surf. Coat. Tech.* **339**, 155–166 (2018).
46. Reddy, G., Lawrence, C. P., Skinner, J. L. & Yethiraj, A. Liquid state theories for the structure of water. *J. Chem. Phys.* **119**, 13012–13016 (2003).
47. Zhang, X., Du, L. & Xu, Z. The effect of soft bake on adhesion property between SU-8 photoresist and Ni substrate by molecular dynamics simulation. *J. Appl. Polym. Sci.* **127**, 4456–4462 (2013).
48. Andersen, H. Molecular dynamics simulation at constant pressure and/or temperature. *J. Chem. Phys.* **72**, 2384–2393 (1980).
49. Darden, T., York, D. & Pedersen, L. Particle mesh Ewald: an N-log(N) method for Ewald sums in large systems. *J. Chem. Phys.* **98**, 10089–10092 (1993).
50. He, Y., Sun, W. T., Wang, S. C., Reed, P. A. S. & Walsh, F. C. An electrodeposited Ni-P-WS₂ coating with combined super-hydrophobicity and self-lubricating properties. *Electrochim. Acta* **245**, 872–882 (2017).
51. Sun, Y. et al. Corrosion resistance of 316L stainless steel in simulated CO₂-bearing crude oil. *Oil Gas Storage Transport* **39**, 0086–0091 (2020).
52. Ding, S. et al. Fabrication of self-cleaning super-hydrophobic nickel/graphene hybrid film with improved corrosion resistance on mild steel. *Mater. Des.* **117**, 280–288 (2017).
53. Zhou, S., Zhu, X., Ma, L., Yan, Q. & Wang, S. Outstanding superhydrophobicity and corrosion resistance on carbon-based film surfaces coupled with multi-walled carbon nanotubes and nickel nano-particles. *Surf. Sci.* **677**, 193–202 (2018).
54. Su, F. & Yao, K. Facile Fabrication of superhydrophobic surface with excellent mechanical abrasion and corrosion resistance on copper substrate by a novel method. *ACS Appl. Mater. Interfaces* **6**, 8762–8770 (2014).
55. Bai, Z. & Zhang, B. Fabrication of superhydrophobic reduced-graphene oxide/nickel coating with mechanical durability, self-cleaning and anticorrosion performance. *Nano Mater. Sci.* **2**, 151–158 (2020).

ACKNOWLEDGEMENTS

This work was supported by Shandong Provincial Natural Science Foundation, China (No. ZR2019MEM014), the Fundamental Research Funds for the Central Universities (No. 20CX02401A) and the Development Fund of Shandong Key Laboratory of Oil & Gas Storage and Transportation Safety.

AUTHOR CONTRIBUTIONS

J.L.: conceptualization, resources, writing—review & editing, funding acquisition. X.F.: validation, investigation, formal analysis, writing—original draft. H.M.: methodology, visualization, data curation. J.C.: investigation, methodology. X.X.: methodology, investigation. G.C.: methodology, resources, supervision. Z.L.: writing—review & editing.

COMPETING INTERESTS

The authors declare no competing interests.

ADDITIONAL INFORMATION

Correspondence and requests for materials should be addressed to Jianguo Liu or Gan Cui.

Reprints and permission information is available at <http://www.nature.com/reprints>

Publisher's note Springer Nature remains neutral with regard to jurisdictional claims in published maps and institutional affiliations.



Open Access This article is licensed under a Creative Commons Attribution 4.0 International License, which permits use, sharing, adaptation, distribution and reproduction in any medium or format, as long as you give appropriate credit to the original author(s) and the source, provide a link to the Creative Commons license, and indicate if changes were made. The images or other third party material in this article are included in the article's Creative Commons license, unless indicated otherwise in a credit line to the material. If material is not included in the article's Creative Commons license and your intended use is not permitted by statutory regulation or exceeds the permitted use, you will need to obtain permission directly from the copyright holder. To view a copy of this license, visit <http://creativecommons.org/licenses/by/4.0/>.

© The Author(s) 2023